Ductile shear damage micromechanisms studied by correlative multiscale nanotomography and SEM/EBSD for a recrystallized aluminum alloy 2198 T8

Xiang Kong[1,*] , Mathias Hurst[2] , Lukas Helfen[2,4] , Fabrice Gaslain[1] , Tilo Baumbach[3] , Heikki Suhonen[5] , and Thilo F. Morgeneyer[1]

[1] *Centre des Matériaux CNRS UMR 7633, MINES Paris, PSL University, 63-65 Rue Henri Auguste Desbruères, 91100 Evry, France*

[2] *Institute for Photon Science and Synchrotron Radiation (IPS), Karlsruhe Institute of Technology (KIT), Hermann-von-Helmholtz-Platz 1, 76344 Eggenstein-Leopoldshafen, Germany*

[3] *Laboratory for Applications of Synchrotron Radiation (LAS), Karlsruhe Institute of Technology (KIT), Kaiserstr. 12, 76131 Karlsruhe, Germany*

[4] *Institut Laue-Langevin, CS 20156 Cedex 9, 38042 Grenoble, France*

[5] *Department of Physics, University of Helsinki, Gustaf Hällströmin katu 2, FI-00014 Helsinki, Finland*

ABSTRACT

The damage mechanisms of ductile fracture under shear loading of an aluminum alloy 2198T8R were studied using flat thin-sheet samples. One sample was loaded until 85% of the failure displacement and then unloaded, and another one was loaded up to failure. To overcome the inherent shortcomings of nanotomography concerning the investigation of flat samples, synchrotron nano-laminography was applied to the pre-loaded sample and provided structural information down to the nanometer scale, allowing ductile damage nucleation and evolution to be studied. The damage features, including flat cracks and intermetallic particle-related damage, were visualized in 3D from the highly-deformed shear band region. Using nano-laminography, no nano-voids were found. The damaged shear ligament was also observed after polishing via destructive correlative scanning electron microscope (SEM) and electron back-scatter diffraction (EBSD) which suggests that the detrimental flat cracks were both intergranular and transgranular. The flat cracks were related to highly-deformed bands. No nano-voids could be found using SEM analysis. Fractography on the second broken sample revealed that the flat cracks contained hardly observable nanometer-sized dimples. The final coalescence region was covered by sub-micrometer-sized dimples, inside which dispersoid particles were present. The fact that no nano-void was found for the pre-deformed sample implies that the nucleation, growth and

---

🖄 Springer

coalescence of these sub-micrometer-sized voids occur at late stages of the loading history.

Introduction

Since the second half of the last century, ductile fracture has been studied at elevated levels of stress triaxiality [1, 2]. Under these circumstances, the nucleation, growth and coalescence of voids have been identified as governing damage micromechanisms [3]. In some cases, high-strength Al alloys may also show intergranular ductile fracture, where ductile damage occurs on a very fine scale by nucleation of voids on grain boundary decorating particles [3]. Ductile damage models describe best the void growth stage for which the stress triaxiality and the plastic strain are identified as driving forces [1, 2]. Under shear, however, the stress triaxiality is close to zero, and classical void growth models do not predict any failure. Since the beginning of this century, research has focused on ductile failure at such low levels of stress triaxiality. Complex relationships between stress triaxiality and strain to failure have been found [4–7]. It has also been identified that the definition of strain to failure is complex and critical. Micromechanistic damage modeling of shear failure often involves the idea of shearing of pre-existing voids that could lead to void rotation, flattening and an associated softening effect [8]. However, few engineering materials contain significant amounts of pre-existing porosity. Fleck et al. [9] studied the effect of a rigid particle on void nucleation and progression in a shear band using FE simulations. They found that accounting for particle matrix contact was important. The case of breaking particles has not been extensively studied numerically but is certainly of interest for Al alloys. Experimentally, the ductile damage mechanisms under shear are not easy to access, as the damage features are not growing substantially. Different methods can be applied to generate locally simple shear [10]. It was found in [11] that increased intermetallic particle content reduced the ductility in shear for a 6XXX series alloy. Through in situ SEM studies, Gross et al. [12] found for an AA6061 T6 alloy void nucleation though particle cracking under shear. Achouri et al. [13] found particle decohesion and void growth around the particle. In such surface studies, the effects of surface preparation, growing surface roughness during the test and neglected 3D effects always question the representativeness of the results.

This makes 3D *in situ* studies appealing. With stick-like in situ tomography samples, it is difficult to do in situ shear loading, particularly for sheet materials. Synchrotron laminography is suited to image regions of interest in large flat samples at micrometer resolution [14–17]. Using in situ microlaminography, Roth et al. [18] observed void nucleation and growth on rigid hard particles in ferrite–bainite steel under shear-dominant loading and validated shear damage phase via a 2D RVE analysis. Voids were nucleated due to particle–matrix decohesion, subsequently elongated and aligned with the principal strain direction. For a ductile Al alloy AA2024-T3, Tancogne-Dejean et al. [19] observed and followed statistically intermetallic particles and pre-existing voids under low stress triaxiality proportional shear loading. It was found that intermetallic particles broke with cracks normal to the principal stress direction. Pre-existing voids were shown to rotate and close, thereby suggesting a limited impact of pre-exisitng voids on failure under shear. Using 2198 T8 recrystallized for in situ microlaminography, the identical material batch as in the present study, Buljac et al. [20] showed that shear damage micromechanisms included detrimental grain-related flat cracks as major damage feature. They also found the second type of damage features: intermetallic particle breakage normal to the maximal stress direction, but with limited effect on the final crack. Void growth was detected during shear since rigid particle debris kept the voids open. Kong et al. [21] performed, again on the same batch as in the present study, load path changes from shear to tension on a cruciform-shaped specimen in AA2198-T8, where the same two main types of damage features were found: grain-related flat crack and intermetallic particle crack. Damage nucleation was observed at the end of shear pre-loading at nearly zero stress triaxiality, and subsequently, the nucleated damage continued to grow and lead to final fracture during tension loading after the shear pre-strain.

The aim of the present work is twofold. One is to identify for the shear loading if the nature of the flat grain-related cracks is intergranular or transgranular. This will be done by a destructive manual sectioning SEM/EBSD study. Another question concerns the sub-micrometer-sized dimples on the final shear fracture

surface as seen in [19]. The question is if the nucleation and growth of these sub-micrometer-sized voids are a gradual process or if it occurs at the very end of the failure process. To identify this, a shear sample test is interrupted at 85 % of the total displacement and scanned by nano-laminography with pixel sizes as low as 100 nm. A second sample, tested up to failure, is investigated by fractography.

Material and methods

Material and sample geometry

An aluminum–copper–lithium alloy 2198 (2.9–3.5 wt.% copper and 0.8–1.1 wt.% lithium) in the recrystallized state after T851 temper condition is chosen in this study. It is referred to as AA2198-T8R in the following. The raw rolled sheet with a thickness of 2 mm was provided by Constellium Technology Center (C-TEC, Voreppe, France). This alloy has a negligible pre-existing porosity (< 0.04 vol%) compared to other aerospace aluminum alloys (e.g., AA2139 in [22] and AA2024 in [19]). The mean volume fraction of intermetallic particles is around 0.34%, and they are shown in white in Fig. 1c. The yield strength is 440 MPa, and the ultimate tensile strength is 500 MPa [23]. Large pancake-shaped grains can be found in the L-T plane in Fig. 1a, with grain size as 82 µm in L, 80 µm in T and 20 µm in S directions (L: rolling direction, T: transverse direction and S: thickness direction). Moderate in-plane plastic anisotropy was found in different loading directions [23], which is consistent with the inverse pole figure in LS plane in Fig. 1b. Moreover, the Lankford ratios ($L_k \approx 0.5 < 1$ [23]), defined as the ratio of the true in-plane

strain in width direction ε_w over the strain through the thickness ε_s, show a significant plastic anisotropy.

A thin sheet of 1-mm-thick material in the so-called *smiley* geometry from [5] was designed and produced for shear loading, where a global tensile loading generates a local shear stress state in two ligaments with dimensions of 1.5×1 mm^2 in Fig. 2b. The dimensions such as notch offset or notch shape have been optimized at the damage location in particular for the AA2198-T8R [5]. Here, 1-mm-thick samples were manufactured from 2-mm-thick raw sheet using electrical discharge machining (EDM).

Nanoscale 3D X-ray synchrotron laminography

Three-dimensional X-ray synchrotron radiation computed nano-laminography allows us to image the regions of interest at very high resolution inside laterally extended samples, in particular in three dimensions [14, 24]. One sample was loaded until failure as shown in black curve in the loading history of Fig. 2a. Another sample was then loaded until of the 85% failure displacement and then unloaded as seen in the blue curve, although it is less than 85% of local strain to fracture according to [20]. One ligament of the deformed sample was cut and imaged with KB mirror-based projection microscopy at the beamline ID16b (ESRF) [25] using nano-laminography [26] with voxel sizes of 236 nm and 48 nm, respectively. They are noted as high resolution (HR) and very high resolution (VHR), respectively. The achievable spatial resolution is limited by the mechanical stability of the nano-laminography setup and corresponds to 135 nm [26]. An X-ray energy of 29.7 keV was employed, and 1500 projections were acquired.
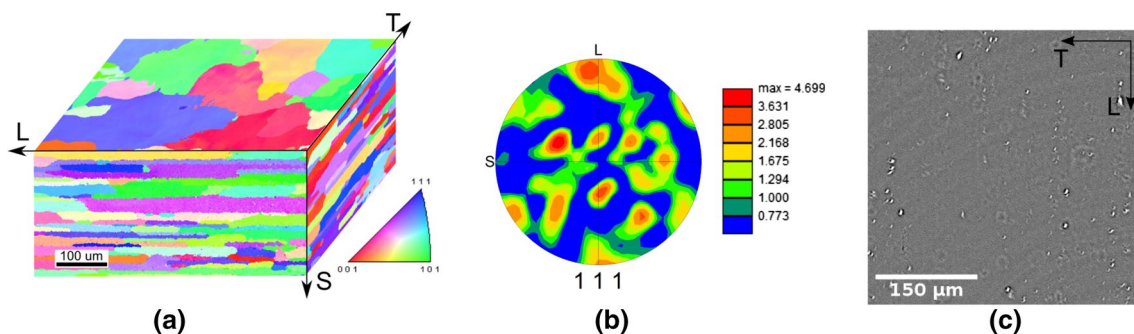

(a)   **(b)**   **(c)**

Figure 1 **a** Inverse pole figure indicating the 3D grain structure of 2198T8R sheet material via EBSD (the crystal orientations are given with respect to the normal of each plane), **b** pole figure of 2198T8R and **c** 2D slice of 2198T8R from high-resolution 3D X-ray laminography in the L-T plane adapted from [23].
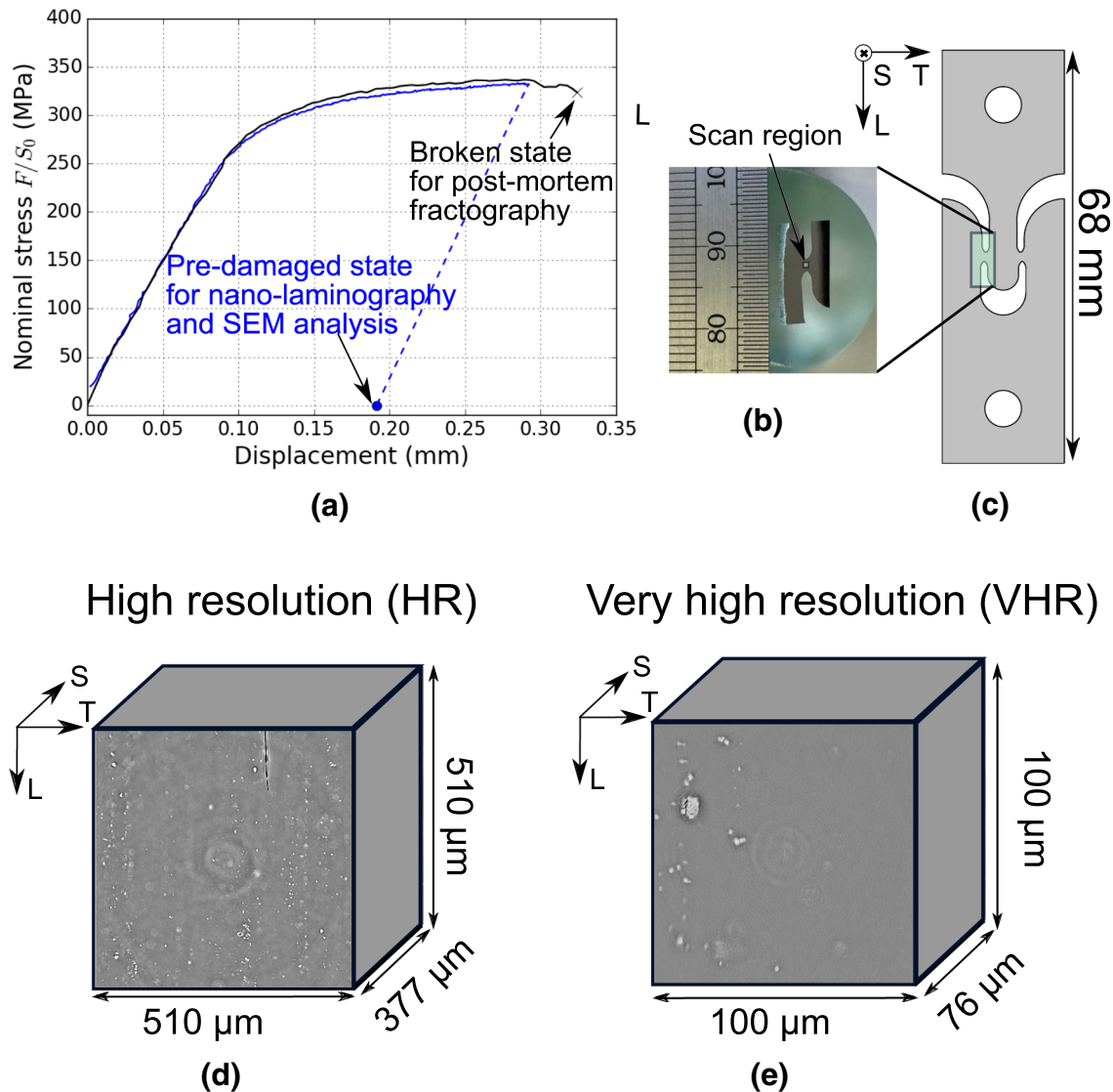
Figure 2 a Load history curve in terms of nominal stress versus displacement. **b** The region of one ligament was cut from **c** the deformed sample for 2D surface observations. Another ligament was investigated by means of 3D nano-laminography at different resolutions: **d** 510×510×377 µm³ as high resolution (HR) with the voxel size of 236 nm and **e** 100×100×76 µm³ as very high resolution (VHR) with the voxel size of 48 nm.

Phase maps have been reconstructed using a non-linear single-distance cone-beam approach from the measured Fresnel diffraction patterns [24], and successive laminographic 3D reconstruction has been performed using the *tofu* framework [27]. Additionally, laminography-specific normalization [28] allowed for an increased reconstruction volume. The final reconstructed volumes have dimensions of 2160×2160×1600 voxels. Two scanned regions are equivalent as 510×510×377 µm³ for HR in Fig. 2d and 100×100×76 µm³ for VHR in Fig. 2e. Both are located in the central part of the highly-deformed shear band region. This was achieved by centering the region of interest using the radiographies of the notches. The shear strain band was measured to be more than 100 µm wide between notches in [20].

Three phases including aluminum matrix in gray, copper-rich intermetallic particles in white and void in black are observed in the laminographic images. For visualization, the data have been segmented and

classified based on the gray value distribution. Damage such as voids and porosity is visualized in blue, while intermetallic particles in gray. The statistics of particle volumes and crack volumes, shown in Figs. 3 and 4, are calculated only from inclusions with volume sizes larger than $1.5\times1.5\times1.5$ µm^3. This reduces the influence segmentation uncertainties due to noise and laminographic artifacts.
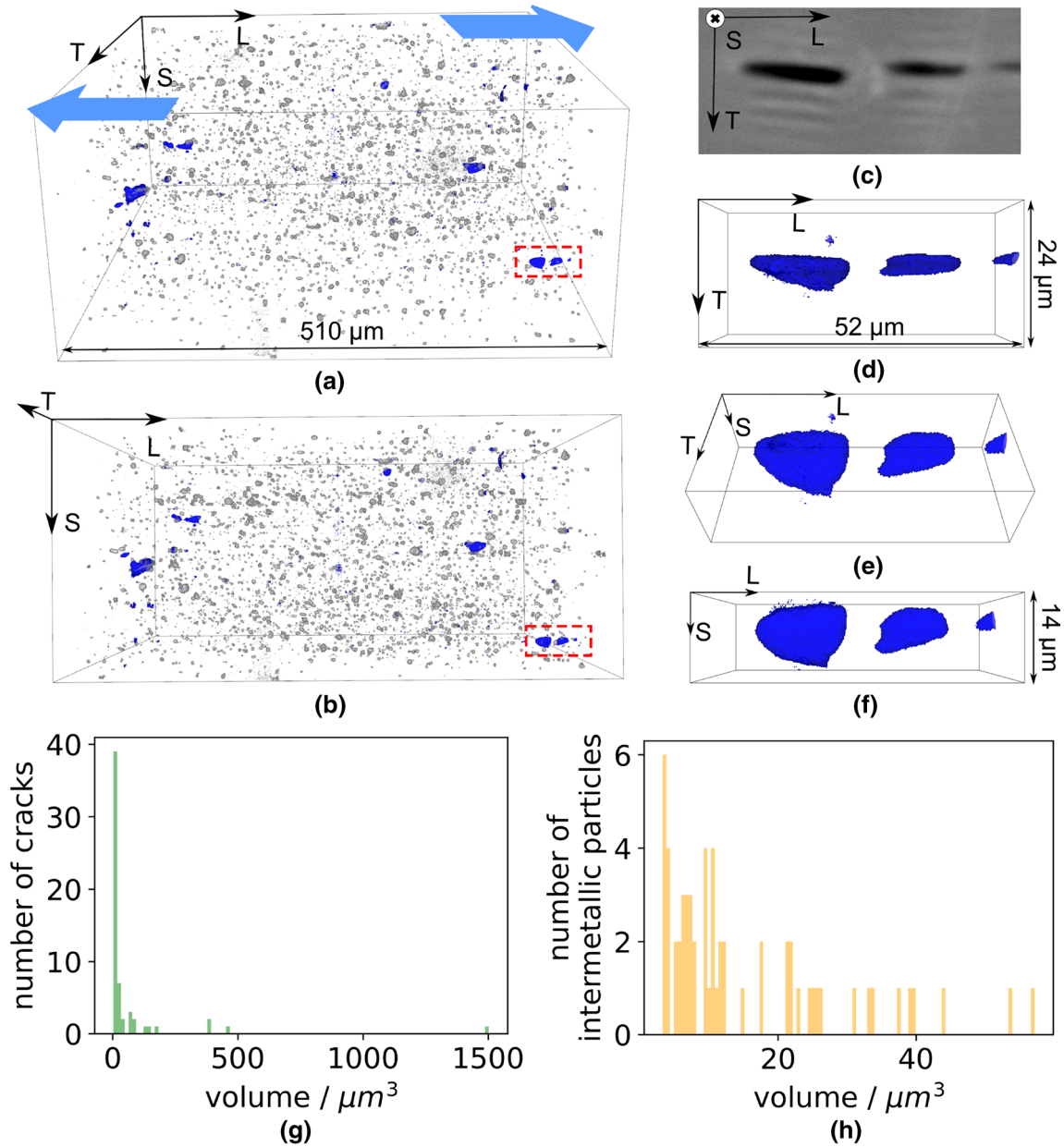

Figure 3 a, **b** Three-dimensional overview visualization of a chosen region of interest (ROI) from the HR scan **c** 2D laminographic slice of a flat crack selected in red box of $52\times24\times14$ µm^3 and its visualization from different views: **d** top view, **e** top-front view and **f** front view with a voxel size of 236 nm. Here, intermetallic particles are segmented in gray and voids in blue. **g**, **h** Size distribution of cracks and intermetallic particles detected in the volume shown in (**a**, **b**).
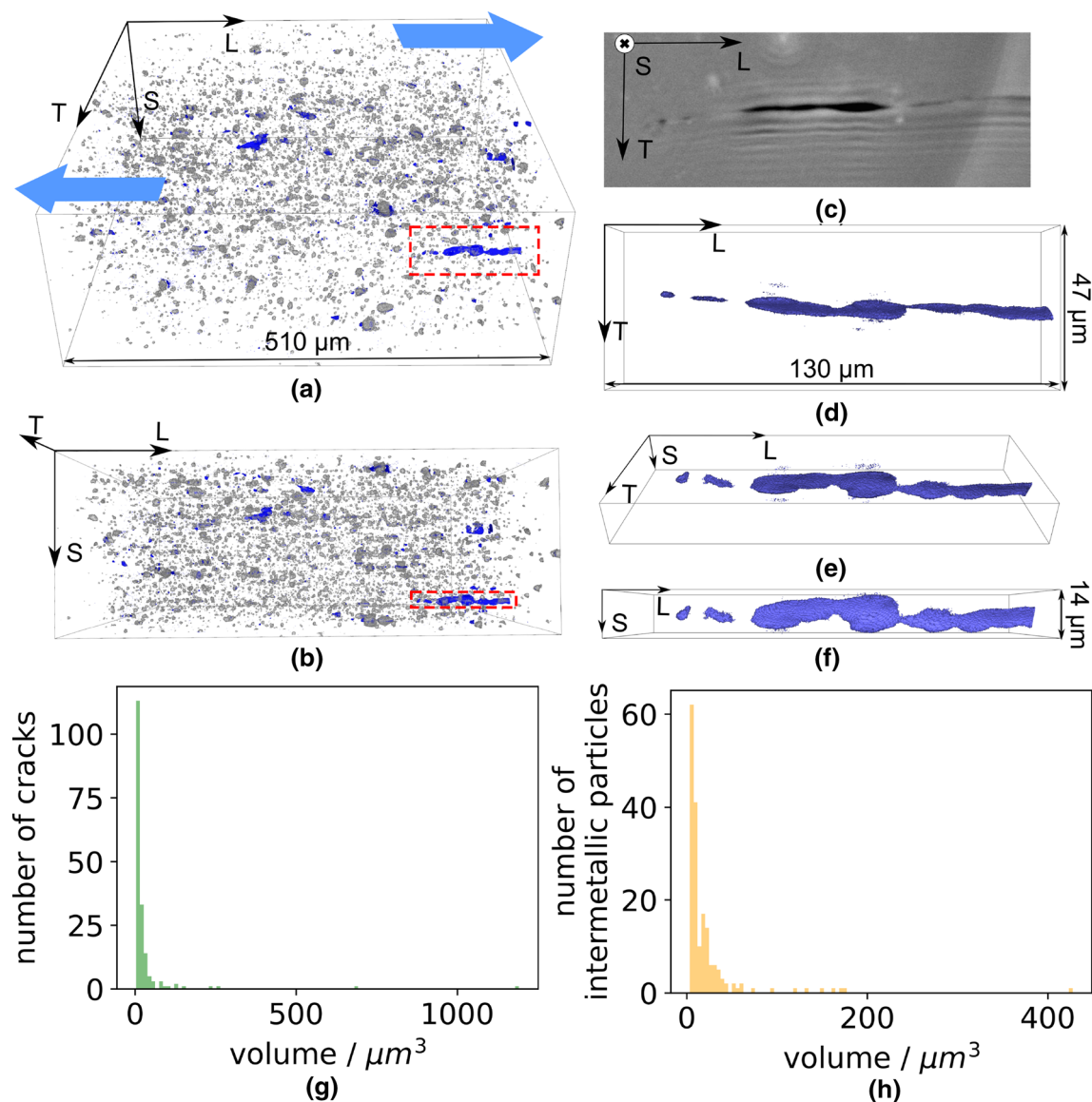
Figure 4 a, b Three-dimensional overview visualization of another chosen ROI from the HR scan. **c** Two-dimensional slice of another long flat crack selected in red box and its 130×47× 14 μm^3 visualization from different views: **d** top view, **e** top-front view and **f** front view with the voxel size of 236 nm. Here, inter-metallic particles are segmented in gray and voids in blue. The wavy structures parallel to the flat crack, visible in (**c**), are artifacts related to the X-ray imaging process. (**g, h**) Size distribution of cracks and intermetallic particles detected in the volume shown in (**a, b**).

Two-dimensional analyses via scanning electron microscopes (SEM) and electron back-scatter diffraction (EBSD)

The fractography was performed via scanning electron microscopy (SEM) in a ZEISS Sigma 300 instrument using a Everhart–Thornley secondary electrons detector. The postmortem surface of the broken sample (black curve in Fig. 2a) was observed on the L-S plane down to sub-micrometer scale.

The planar (L-T) features on surface of the deformed specimen were observed in a FEI Nova NanoSEM 450. Orientation maps of grain structures were obtained from electron back-scatter diffraction analyses with an EDAX-TSL Hikari camera and the OIM software using a step size of 0.5 μm and an acceleration voltage of 15 kV. A grain boundary is considered when the

misorientation angle between the two grains is less than 15°.

The surface of the deformed sample was polished incrementally (in a destructive way) until damage features appeared. Considering the dimensions of damage features, which were measured as less than 20 μm in the 3D imaging and in order not to remove them, a 10 μm thick material layer was removed for each polishing step. The surface was polished gradually using 7 μm down to 3 μm and 1 μm polishing paste.

Results

Two volumes of *ex situ* nano-laminography exhibit the 3D morphology of damage features inside the deformed sample at high resolution (HR) and very high resolution (VHR). The damage features from the ligament were studied in a correlative way via additional 2D observations by SEM and EBSD.

Nano-laminography observations of the damaged sample under shear

The microstructural features such as flat cracks and particle cracks were found under shear using the micrometer scale computed laminography in [20, 21]. They are likely to strongly contribute to the final macro-fracture under shear loading. The 3D overview visualizations of the deformed sample from high-resolution (HR) nano-laminography on two 510×510× 188 μm^3 volumes close to the mid-thickness plane are shown in Figs. 3a, b and 4a, b, where void in blue and particles in gray. The two main damage features: flat crack and particle crack, are both visualized as void in blue.

Flat crack observed at high resolution (HR)

It is worth emphasizing that this shear-induced feature has not been observed before in the same geometry for other alloys (FB600 steel in [18], AA2024T3 in [19]). In order to observe this detrimental damage feature, a flat crack was selected in the red box having a size of 52×24×14 μm^3 in Fig. 3a and b. The 2D slice of the crack is given in (c). The segmented crack is visualized in (d-f) different 3D views to specify the damage mechanism in the deformed state. Three flat micro-cracks with 15 μm length, 5 μm width and 10

μm thickness were found. They are believed to grow and coalesce to a larger flat crack up to 50 μm length at the next stage, according to [19–21]. In addition, there is no particle adjacent to the crack, which indicates that the crack probably does not nucleate on a particle.

Another longer flat crack is chosen in Fig. 4a and b in red frame. The subvolume of 130×47×14 μm^3 exhibits a coalesced flat crack feature in (c-f) at a later stage compared to the previous one. The length of this damage feature is up to 100 μm, and its width is less than 10 μm as well as 14 μm thick, which is close to the grain size of the present material.

Besides the described long cracks, the volumes contain smaller cracks. The volume distributions of these cracks are shown in Figs. 3g and 4g. It can be seen that there is a large number of small damage features (having volumes ≤ 500 μm^3) and very few large cracks (having volumes of 1000–1500 μm^3). As shown in Figs. 3h and 4h, the volumes of the intermetallic particles are much smaller (having volumes of 50–200 μm^3). For the statistical analysis, only features with average volumes larger than 1.5×1.5×1.5 μm^3 have been taken into account to avoid a bias due to noise and laminographic artifacts.

Particle crack observed at very high resolution (VHR)

The fracture of the secondary phase intermetallic particle is the second type of damage feature during shear loading. The lengths of damaged particles range from a few micrometers up to 10 micrometers. Thanks to the very high-resolution (VHR, voxel size down to 48 nm) nano-laminography on the deformed sample, the particle-related features including particle breaking and particle–matrix decohesion were segmented and visualized in different views. The feature of detrimental flat crack was not captured in the small field of view of VHR scan.

A damaged particle having an ellipse shape of 5 μm diameter is shown in the 2D slice of Fig. 5a, b, and a subvolume of 12.2×11.5×9.6 μm^3 is visualized in different top views in (c) and front-top views in (d). The particle was broken in the middle under shear. Another particle with a similar shape and size as 5 μm length is selected in (f) from (e) the 2D section. The shear loading direction is illustrated in blue. The 3D visualizations inside the subvolume as 5.8×5.8×4.0 μm^3 present the particle damage linkage to the particle–matrix decohesion in Fig. 5g and h.

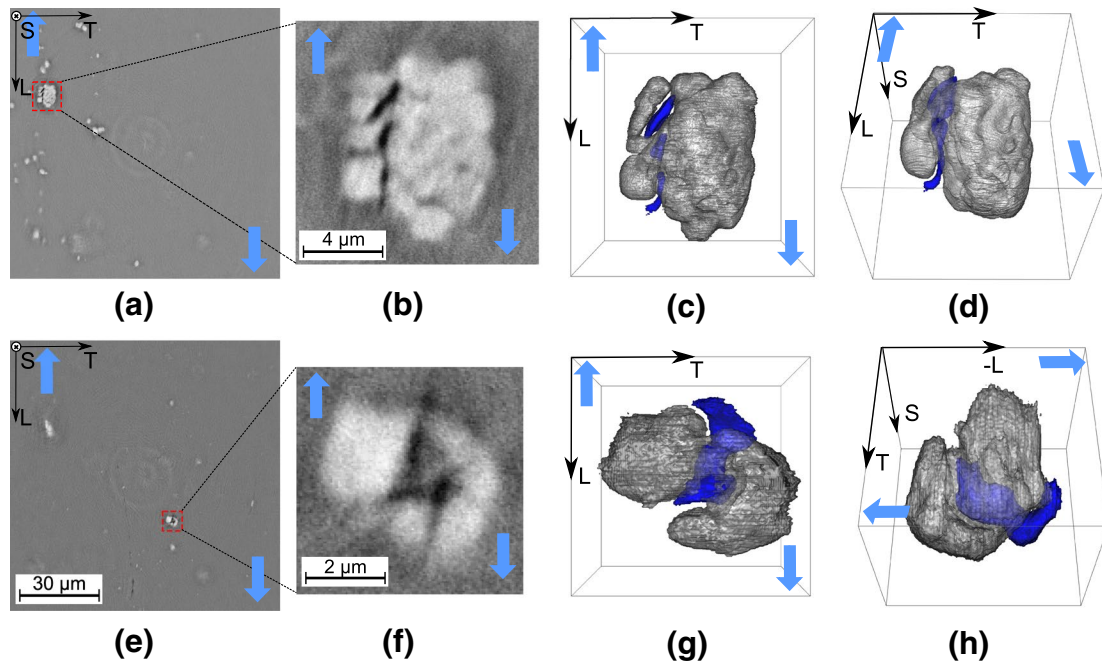**Figure 5** Intermetallic particle damage feature of **a** 2D slice and its **b** detailed ROI with a size of 12.2×11.5×9.6 μm^3 from different views: **c** top and **d** front-top views. **e** Two-dimensional slice and **f** its selected ROI with a size of 5.8×5.8×4.0 μm^3 from different views: **g** top and **h** right-top views, where the shear loading direction is indicated in blue.

Two broken particles around micrometer length are exhibited in Fig. 6b and e. The rigid particles were likely to rotate and break into debris by the evidence of in situ data [19, 20]. Figure 6c and d presents the visualizations of the 6.4×8.2×3.4 μm^3 sub-region including a particle in triangular shape of 2 μm. The particle

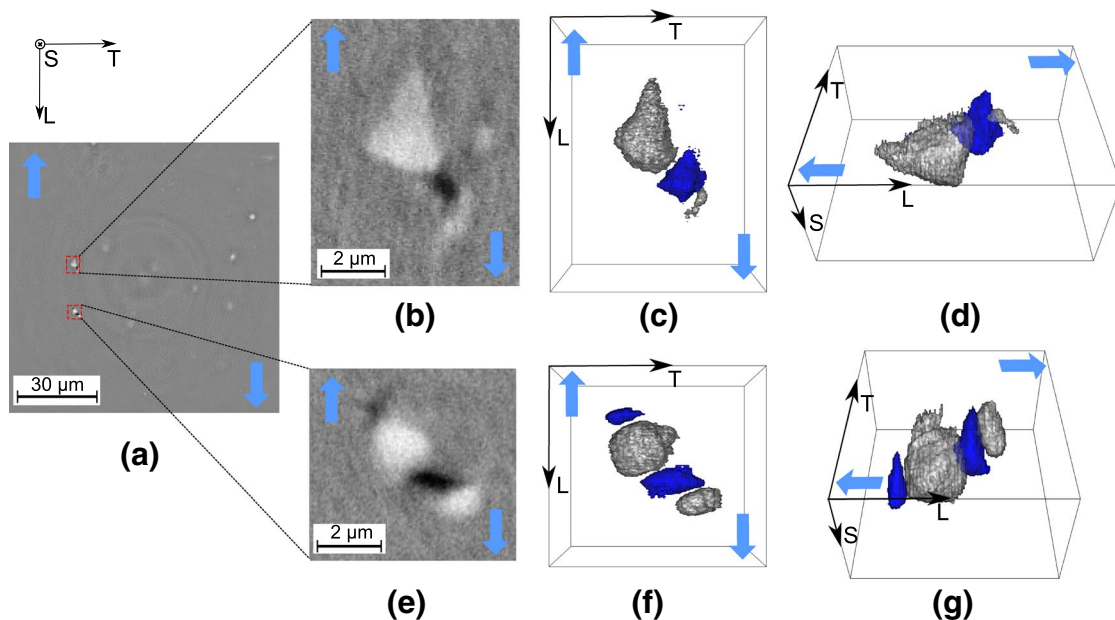**Figure 6** Intermetallic particle damage feature of **a** 2D slice and its **b** detailed ROI with a size of 6.4×8.2×3.4 μm^3 from different views: **c** top and **d** left-top views. **e** Two-dimensional slice and **f** its selected ROI of 6.2×5.8×3.4 μm^3 from different views: **g** top and **h** left-top views. The space between particles and voids is linked to segmentation uncertainties.

fractured at the lower position under loading and the porosity appeared as a small part of the particle was separated. The tiny piece was torn apart before fracture in (e). After the particle was broken, the cavities probably grew under local shearing. The voids and particle debris are visualized in Fig. 6f and g. The void growth under shear is possible due to the rigid nature of the particles that keep the voids open.

Microstructural origin of flat cracks studied by SEM and EBSD

For the second ligament of the deformed specimen in Fig. 2c, the surface was polished incrementally and thereby in a destructive way until damage features appeared for correlative SEM and EBSD observations.

Origin of the flat cracks

The size of the detrimental damage features, flat cracks, ranges from several micrometer to 20 μm length and was observed in the region of interest via SEM. Since none of these cracks is linked to intermetallic particles, their nucleation might correspond to grain boundaries or slip bands regarding their dimensions. In order to verify the crystallographic relationship, these surfaces were assessed by EBSD analyses.

Flat cracks are observed and labeled in Fig. 7. These cracks were measured as around 10 μm in length and less than 3 μm in opening. Each flat crack was noted as F plus the index as illustrated.

These flat cracks are found to be located on the grain boundaries (i.e., intergranular) in Fig. 8b and d via EBSD. In addition to these flat cracks, several localized bands in dark gray along the loading direction are visible in the highly shear deformed region of 100 μm width. The flat cracks F1, F2, F3 and F4 are exactly situated on these strain localization bands proved by (e) kernel average misorientation (KAM) figure. Interestingly, the orientation of these bands changed abruptly within the "purple" grain seen in Fig. 8b, which proves that they are probably slip bands. The two flat cracks named after F5 and F6 in Fig. 9 are proved to be intergranular by EBSD as well.

Other flat cracks of similar dimensions are found within grains as transgranular damage in Fig. 10. The flat crack cluster is observed in Fig. 10a as F7 cluster and other two flat cracks F8 and F9 shown in Fig. 11b. The inverse pole figures of three different crystal directions indicate that these linear damage features lied both between grains of very close orientations in three axes in (c-e), and thus, they are probably transgranular.

The detrimental damage features, flat cracks, are identified as half intergranular and half transgranular
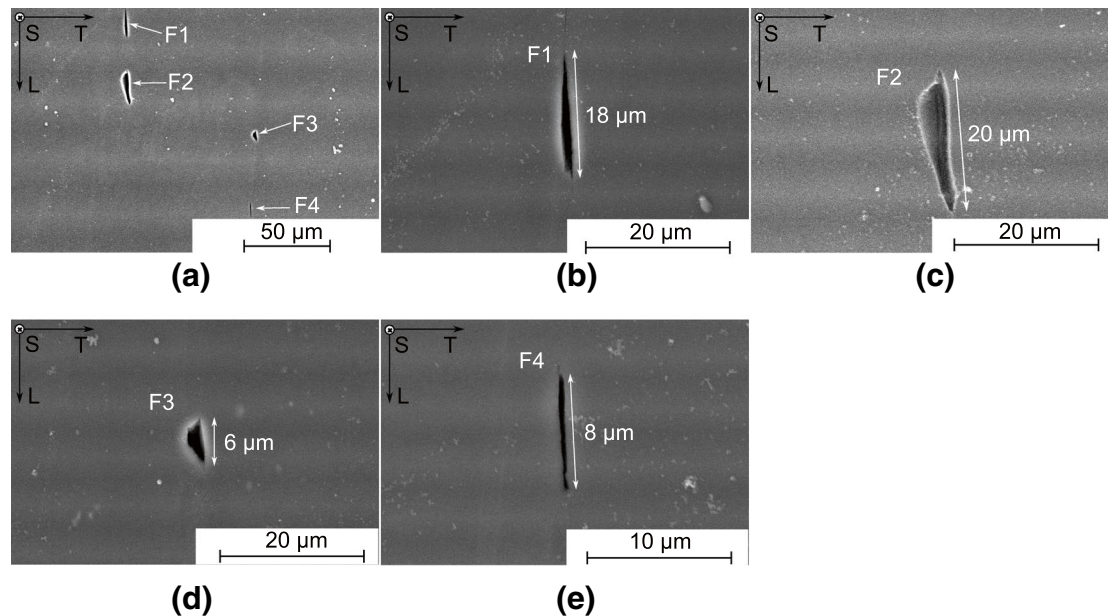

Figure 7 Damage features of flat cracks observed by scanning electron microscopy (SEM): **a** four flat cracks noted as **b** flat crack 1 (F1), **c** F2, **d** F3 and **e** F4 on one surface.
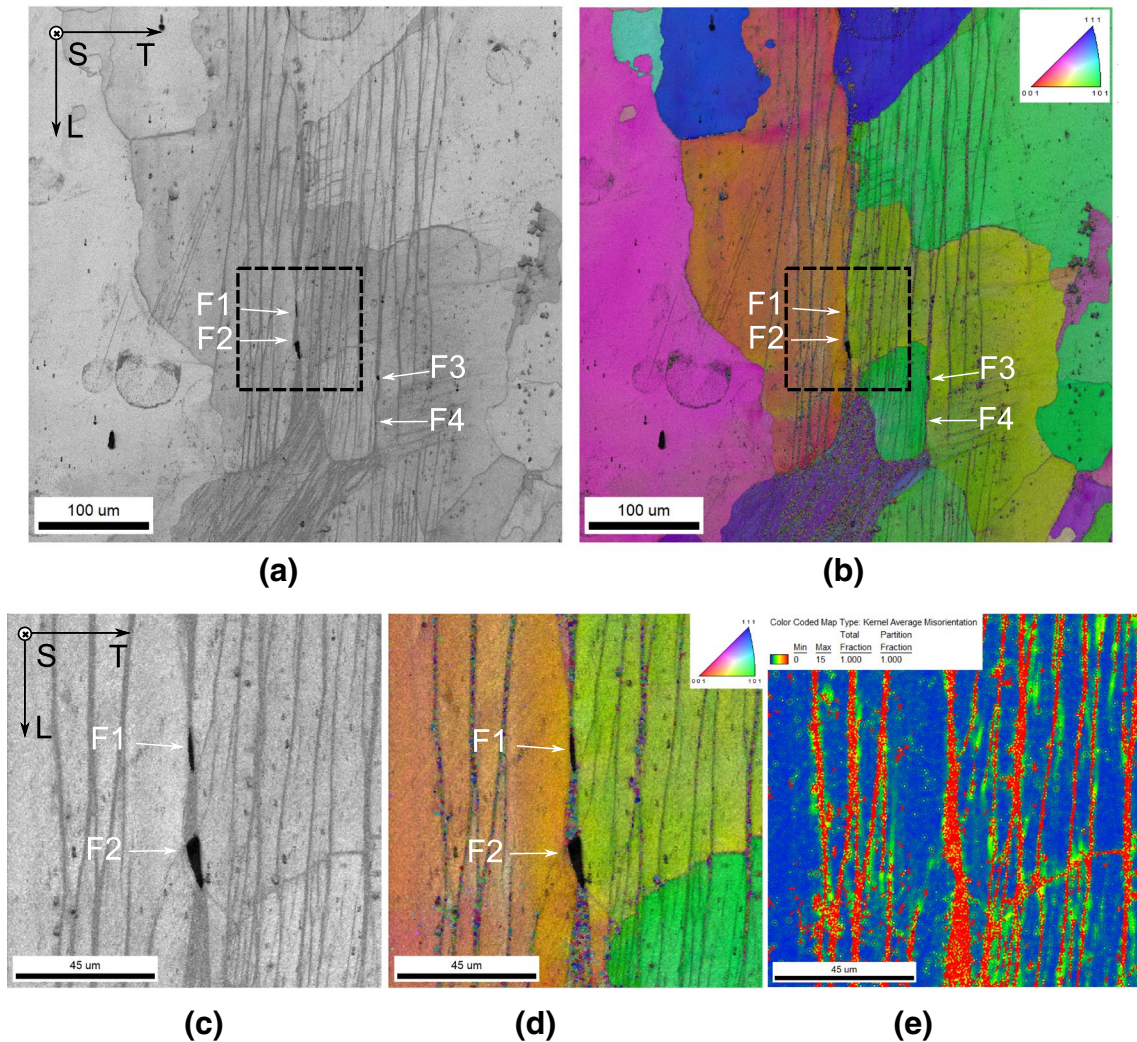
Figure 8 The intergranular flat cracks in Fig. 7 via EBSD analysis. Gray scale maps: image quality figures (**a**, **c**) and their related color-coded maps: inverse pole figures (**b**, **d**), where (**c**, **d**) present the zoomed region of (**a**, **b**), respectively. **e** Kernel average misorientation (KAM) figure of the zoomed region.

with the information, tediously obtained in this study. It is assumed that the flat cracks could grow and coalesce to longer features up to 100 μm length as shown by laminographic 3D imaging that led to the final failure.

Intermetallic particle cracks

The other important damage features under shear are the intermetallic particle cracks. Figure 12 shows the cracks nucleated within the deformed particles of sizes less than 10 μm × 10 μm via SEM observations. Three ellipse-shaped intermetallic particles in Fig. 12a, b, d and a stick-shaped one in (c) were found with cracks inside. They probably rotated with respect to the rolling direction [20]. The crack opening orientation of four particles is similar after rotation. As the major damage feature in AA2024 [19] and AA2198 [20], they found the particle failures oriented normal to the principal stress orientation. The void stays open (i.e., void locking) because the second-phase particles are rigid. The aluminum matrix seems to flow into the voids from both sides in Fig. 12d, consistent with the low levels of stress triaxiality.
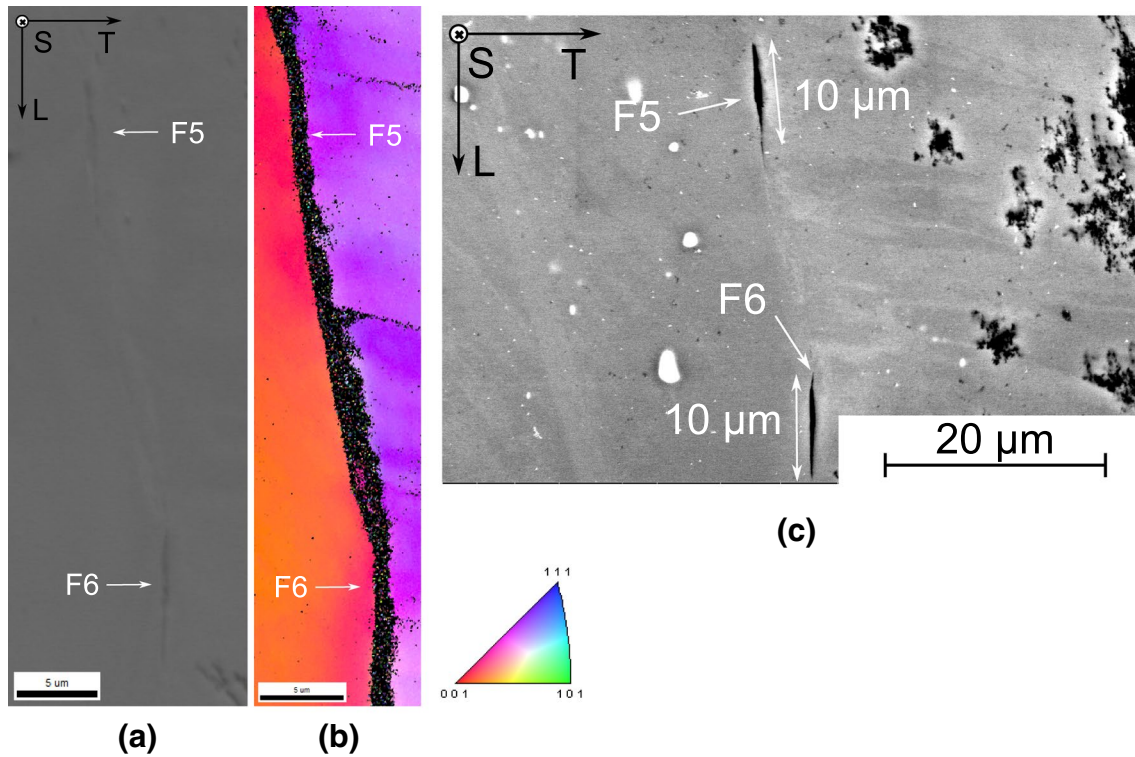
Figure 9 **a** Two flat cracks F5 and F6 on another surface where some dirts are included in the right in (**c**). The flat cracks are proved to be intergranular in (**b**) via EBSD analysis.

Discussion

Fracture mechanism under shear for AA2198T8R

Negligible amounts of pre-existing voids (less than 0.04% in [29]) are found in AA2198T8R. If voids are present in the material, they were seen to elongate and close under shear, as shown in AA2024T3 [19]. Importantly, the hydrostatic pressure as a main driving force under shear loading is missing for void growth.

The evolution of each damage feature was illustrated in [20] from in situ micro-laminography for AA2198T8R. The nucleated flat cracks grew and coalesced to a longer crack, acting as a trigger for the final macro-crack. Meanwhile, strong but brittle intermetallic particles rotated and then either broke or decohered from the matrix, both resulting in voids in the material. This is one of the main damage features for AA2024T3 under shear [19]. Besides, due to a relatively high pre-existing porosity (0.7%) for AA2024T3, the deformation of the pre-existing voids was continuously controlled by the matrix rotation and not prone

to any sudden event, even under large deformations. Roth et al. [18] found that decohesion at the interface between the particles and matrix leads to void growth and micro-crack formation under shear for FB600 steel, whose initial porosity was also negligible down to 0.05% as AA2198T8R in this study.

In this work, the nucleation of this detrimental flat crack feature was studied via 3D and 2D high-resolution techniques. The observed flat cracks were proven to originate from the grains or grain boundaries rather than intermetallic particles. Indeed, two flat cracks were proved to be intergranular in Figs. 8 and 9 while another two flat cracks were found within the grains (transgranular) in Figs. 10 and 11 via EBSD analysis. The shear bands were found in the highly localized region in Fig. 8c, d, and these localized bands probably resulted in the transgranular flat cracks. It would be interesting to have more statistical data, but the information is extremely hard to obtain.

Figure 13 suggests the shear damage mechanism schematically in damage state. It schematizes the two main features: flat cracks (green and red) and particle cracks (yellow). The former feature is more
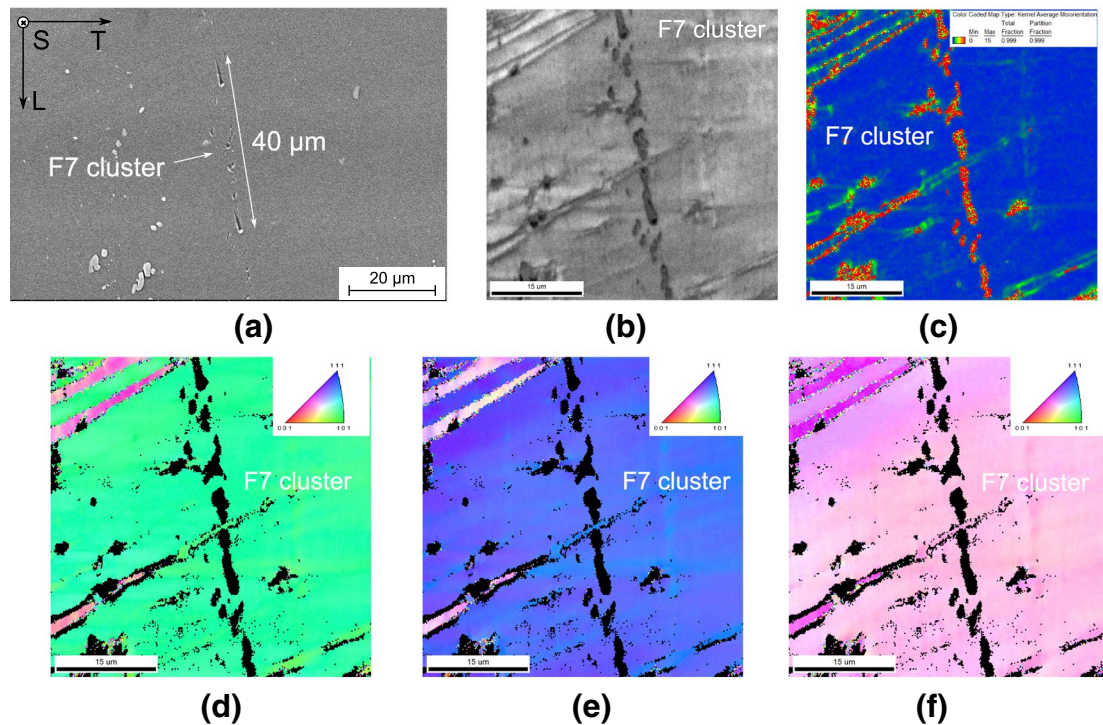
Figure 10 Damage feature of transgranular flat cracks via SEM: **a** a cluster of flat cracks noted as F7 cluster on surface. **b** The zoomed-in region and **c** ker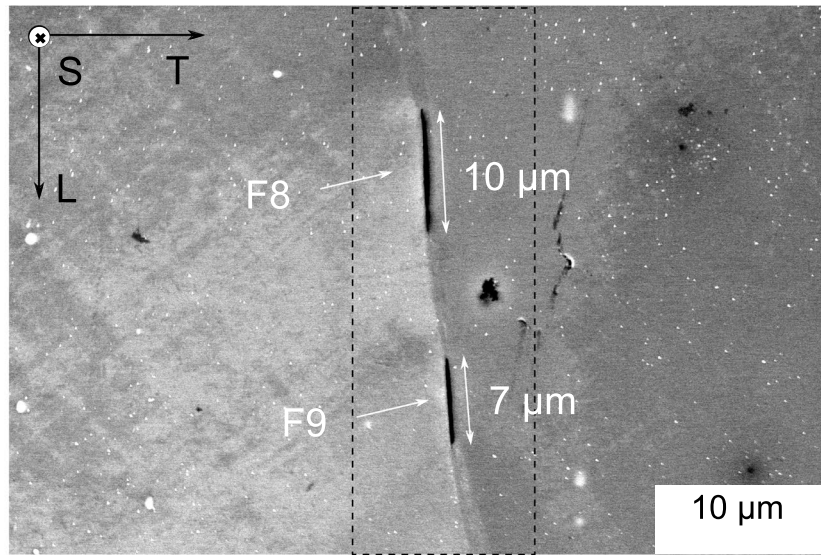nel average miorientation (KAM) fig-ure. The cluster of flat cracks are proved to be transgranular via EBSD analysis in inverse pole figures of three **d** [100] **e** [010] **f** [001] crystal directions.

detrimental, which could be identified by correlative EBSD and proved as transgranular crack (green) initiated on the localized shear bands in (a) and intergranular crack (red) initiated on the grain boundary in (c). The second type of damage features, which is the main damage feature for AA2024T3 [19] and for FB600 steel [18], is related to secondary phase intermetallic particles. Two particle-related cracks are shown in (d-e), where particles rotated and broke into debris to open voids.

The scheme in broken state is shown in Fig. 14 from (a) L-T and (b) L-S plane. From the fracture surface, there are two main regions: (1) the detrimental flat crack and particle-related crack, (2) the smooth region with typical shear dimples in pink. The thickness (S) of flat cracks can grow to more than 20 μm as observed in (e) while the length (L) can be up to 100 μm in Fig. 4, which is consistent with the grain size. The stretched micrometer-sized dimples are found only next to flat cracks and not found on the crack itself in (d-f). In the flat cracks, they are even smaller nano-sized dimples. At the high resolution down to nanometer, localized bands are found on the side wall of flat cracks in (f). On the bottom of the flat crack, a smooth surface with

the oriented and stretched feature is observed and zoomed-in (d). The detrimental features are probably initiated on the grain boundary or localized strain bands. Secondly, the shear dimples were found from sub-μm up to a few μm in length with nano-dispersoids (white dots in (c)(g) and schematically in (b)) around 100 nm. The microscopic shear dimples might initiate on these nano-dispersoids during final coalescence. This is supposedly happening during the final unstable fracture where sub-micrometer void nucleation, growth and coalescence happen almost simultaneously for a very small (or even no [30]) macroscopic machine displacement. Neither in the nano-laminography observation nor for the SEM observation during serial sectioning, damaged dispersoids were found.

The damage evolution was quantified as surface void fraction in [20, 21] since the detrimental flat cracks have a very low void volume fraction. The surface void fraction grew steadily up to only 3% even the maximum equivalent strain reached more than 0.6. Current models under shear-dominated loading [8, 18] assume that shape changes of pre-existing voids or decohesion of rigid particle rather than void nucleation without the presence of particles (e.g., flat cracks). A
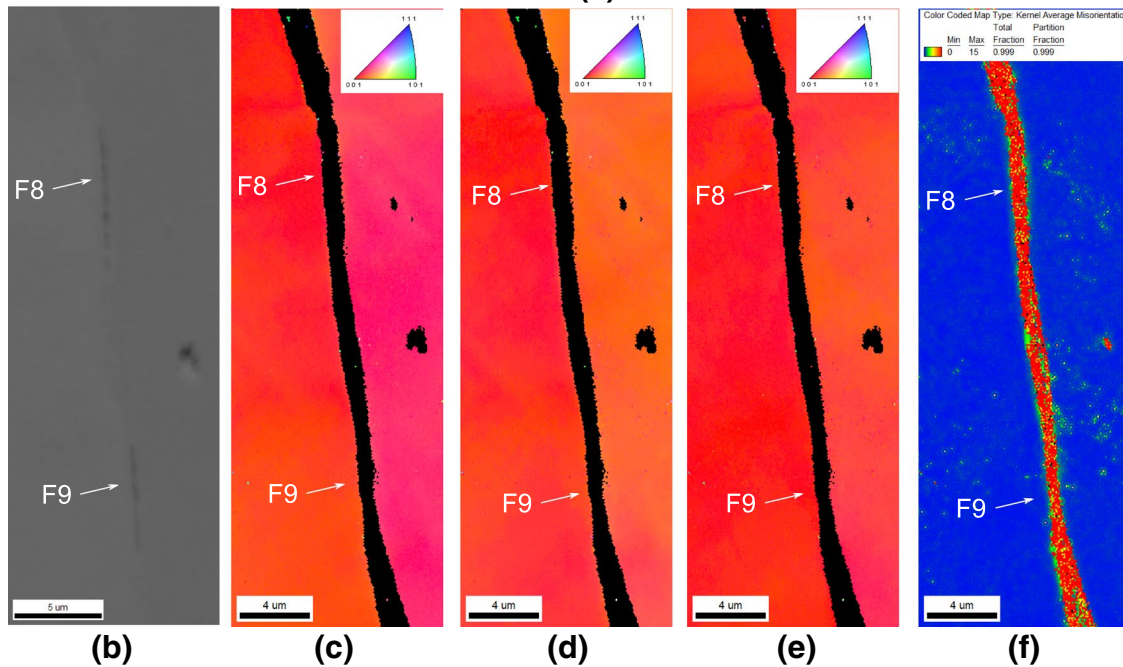
Figure 11 Damage feature of transgranular flat cracks via SEM: **a** two flat cracks named F8 and F9 (cropped in **b**) are proved to be transgranular via EBSD analysis in inverse pole figures of three **c** [100] **d** [010] **e** [001] crystal directions and **f** kernel average misorientation (KAM) figure.

mechanism-based ductile model [31], which fully couples classical void growth at high stress triaxiality and Coulomb fracture model at the slip system scale at low stress triaxiality (shear), could be applied to predict the proportional shear loading and even non-proportional load path changes. A reduced texture methodology (RTM) was used to provide computational efficiency, and this approach involved a significant reduction of the number of representative crystallographic orientations. The damage nucleation along slip planes could represent the observed generation of shear flat cracks. This has been attempted in [32].

Figure 12 The damage feature of intermetallic particle cracks via SEM: **a**, **b**, **d** ellipse-shaped and **c** stick-shaped particles.
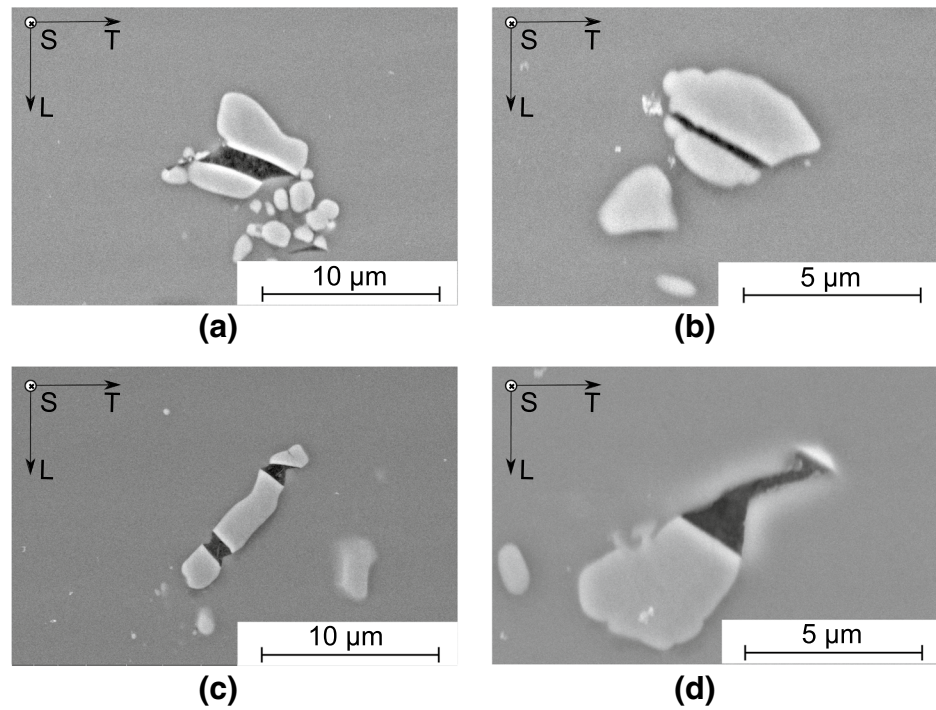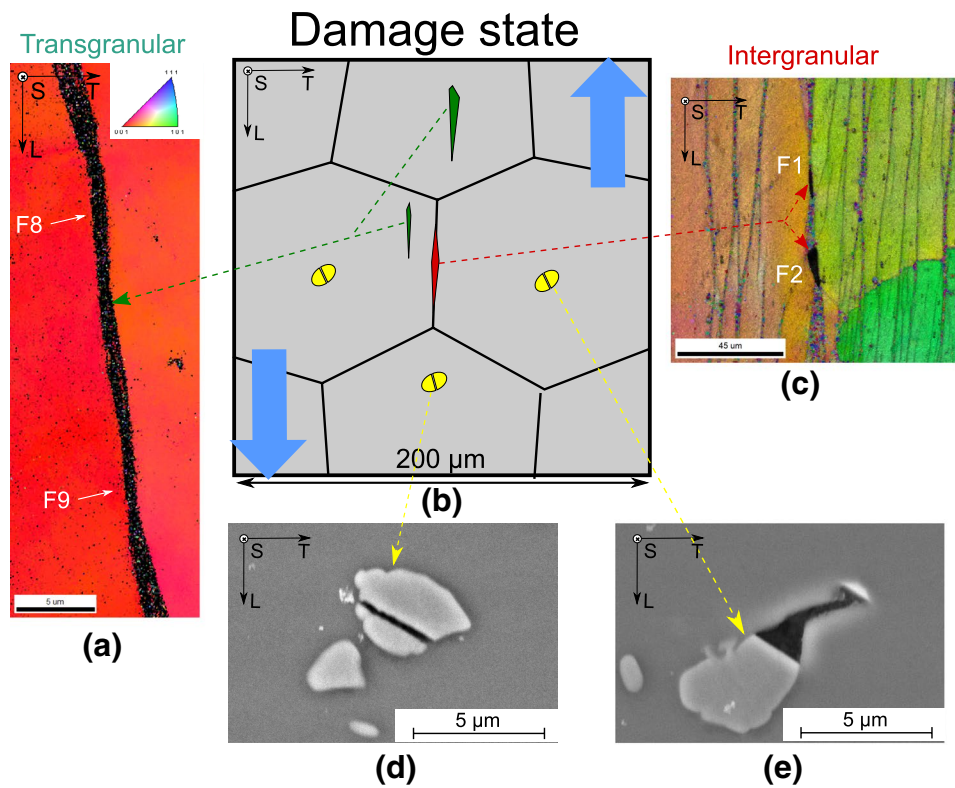

(a)

(b)

(c)

(d)

Figure 13 **b** A schematic shear damage mechanism demonstration in damage state with damage feature-evidence on LT plane via SEM observations: **a**, **c** flat cracks and **d**, **e** particle cracks.
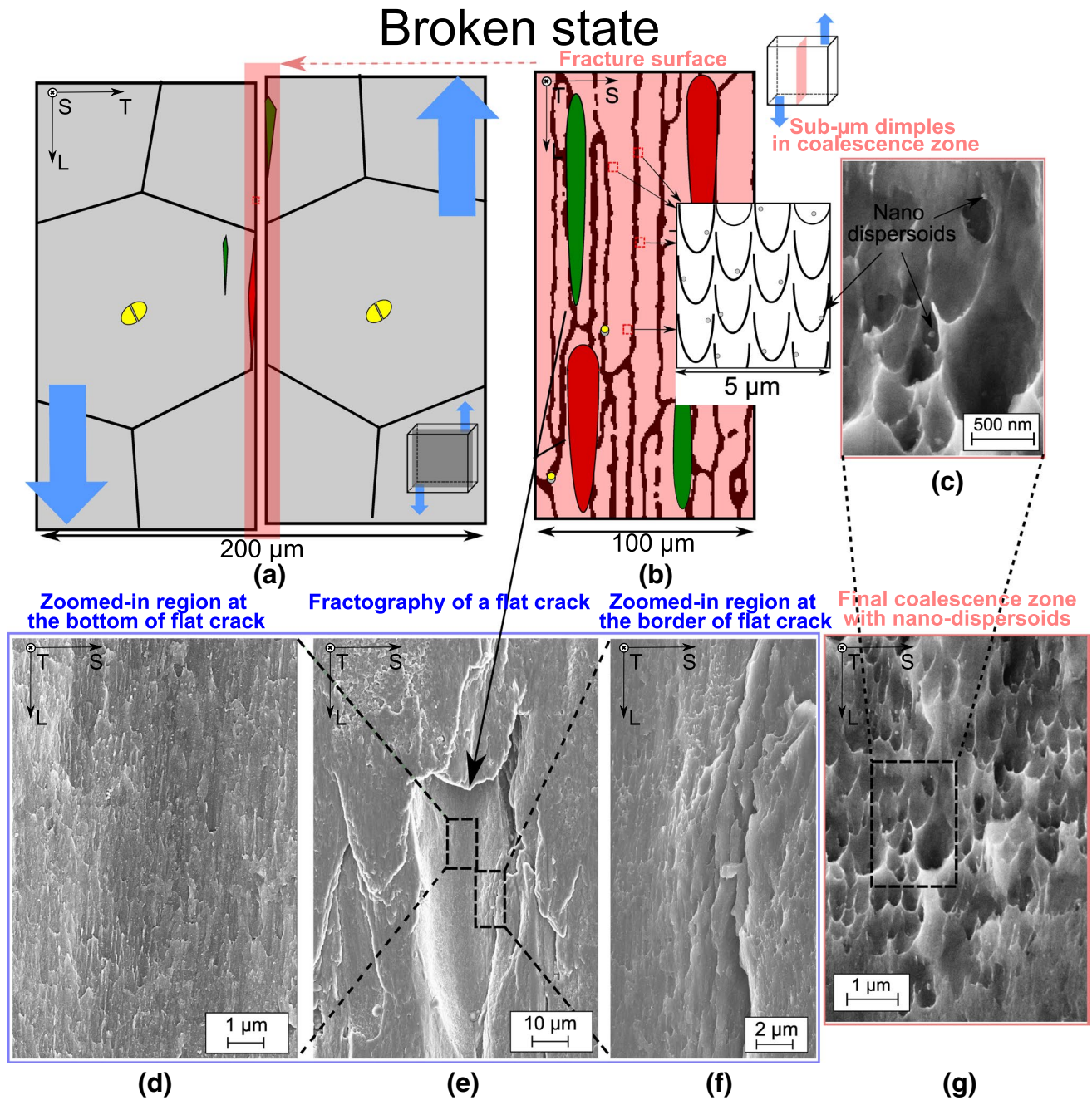

Transgranular

Damage state

Intergranular

F8

F9

F1

F2

200 μm

(a)

(b)

(c)

(d)

(e)

Figure 14 A schematic shear damage mechanism demonstration in broken state from **a** LT plane and **b** LS plane of EBSD grain boundary outlines, as well as SEM fractography of a second sample: **d** the zoomed-in region of **e** a flat crack and **f** the zoomed-in region at the border of the flat crack with no observable dimples. **c** The zoomed-in region of (g) final coalescence zone with nano-dispersoids.

Conclusion

The damage nucleation under shear was studied for an AA2198T8R alloy using a sample obtained by an interrupted shear test and a broken sample. From the correlative 3D nano-laminography and destructive 2D SEM/EBSD observations, two main types of damage features under shear were identified: grain-related flat cracks and intermetallic particle cracks. The former, whose direction is parallel to the loading

direction (L), plays a major role in the final failure [20]. The length can be up to 100 μm, and this feature has not been observed so far in other alloys under shear [18, 19]. Both damage features were observed down to the nanoscale via *ex situ* nano-laminography at high resolution (HR) and at very high resolution (VHR) as well as via EBSD analysis after polishing to study the link of the flat cracks to the granular microstructure. SEM fractography helped to understand the final shear damage mechanism.

The principal conclusions can be drawn as follows:

- Two main damage features, flat cracks and intermetallic particle cracks, were found in AA2198T8R under shear loading. The former is supposedly more detrimental as it covers relatively large regions of the fracture surface.
- The detrimental flat cracks do not nucleate on the intermetallic particles, and the gathered EBSD data after successive polishing suggest that they are both intergranular and transgranular. The flat damage is located in the highly-deformed region in the localized bands or grain boundaries.
- The intermetallic particles either break or decohere from the aluminum matrix, eventually leading to nucleation of voids and even growth, as the stiff particles keep the voids open (i.e., void locking).
- The sub-micrometer-sized shear dimples were found in most of the smooth areas of fracture surface, which might initiate on the nano-disperoids during final coalescence associated to unstable fracture. The fact that no damaged dispersoids were found for the pre-strained sample suggests that damage nucleation on dispersoids occurs at late stages of deformation.

Acknowledgements

Author contributions

TB, TFM and LH helped in conception and design of study; XK, MH, LH, FG and HS helped in acquisition of data; XK, MH, LH, FG and TFM helped in analysis and/or interpretation of data; XK, MH and TFM contributed to writing of the original draft; MH, FG and TFM helped in revising the manuscript critically for important intellectual content and XK, MH, LH, FG, TB, HS and TFM helped in approval of the version of the manuscript to be published.

Funding

Data availability

All necessary data generated or analyzed during this study are included in this published article, and other auxiliary data are available from the corresponding author on a reasonable request.

Declarations

Conflict of interest The authors declare that they have no known competing financial interests or personal relationships that could have appeared to influence the work reported in this paper.

Appendix

Finite element simulation

The finite element method offers the access to the stress state (e.g., stress triaxiality). Due to geometry symmetry, a quarter of the sample (half thickness and half width) was meshed using quadratic hexahedral elements (c3d8). The displacement is applied to the edges vertically, which generates the shear state in the ligament between notches. The material in this study was characterized and modeled using an elasto-plastic behavior with isotropic hardening and a yield criterion for plastic anisotropy [23]. The simulation was performed using the in-house finite element software Z-set [33].
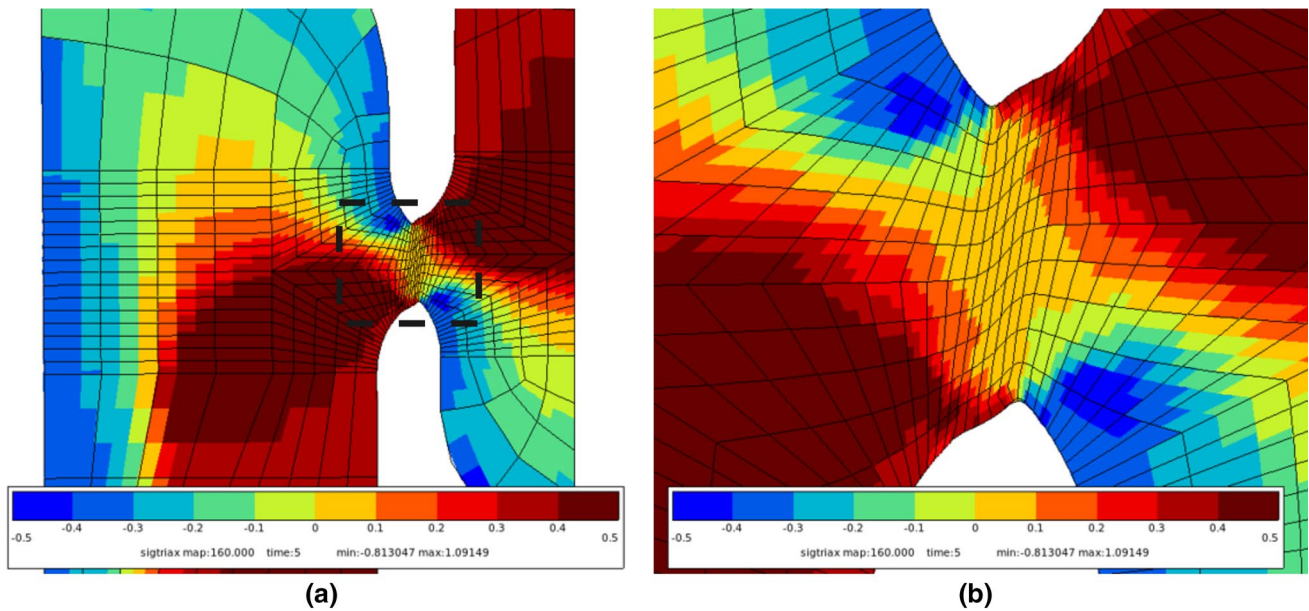
Figure 15 Stress triaxiality field in **a** the quarter of the geometry and **b** the highly-deformed region zoomed-in from the black square in (**a**)

Figure 15 presents the stress triaxiality field under shear loading when the vertical displacement is 0.3 mm. The nearly zero value between notches confirms the shear-dominated stress state in the highly-deformed region as seen in (b).

References

[1] Rice JR, Tracey DM (1969) On the ductile enlargement of voids in triaxial stress fields. J Mech Phys Solids 17:201–217. https://doi.org/10.1016/0022-5096(69)90033-7

[2] McClintock FA (1968) A criterion for ductile fracture by the growth of holes. J Appl Mech 35:363–371. https://doi.org/10.1115/1.3601204

[3] Garrison WM, Moody NR (1987) Ductile fracture. J Phys Chem Solids 48:1035–1074. https://doi.org/10.1016/0022-3697(87)90118-1

[4] Bao Y, Wierzbicki T (2004) On fracture locus in the equivalent strain and stress triaxiality space. Int J Mech Sci 46:81–98. https://doi.org/10.1016/j.ijmecsci.2004.02.006

[5] Roth CC, Mohr D (2016) Ductile fracture experiments with locally proportional loading histories. Int J Plast 79:328–354. https://doi.org/10.1016/j.ijplas.2015.08.004

[6] Barsoum I, Faleskog J (2007) Rupture mechanisms in combined tension and shear-experiments. Int J Solids Struct 44:1768–1786. https://doi.org/10.1016/j.ijsolstr.2006.09.031

[7] Papasidero J, Doquet V, Mohr D (2015) Ductile fracture of aluminum 2024–t351 under proportional and non-proportional multi-axial loading: Bao-wierzbicki results revisited. Int J Solids Struct 69:459–474. https://doi.org/10.1016/j.ijsolstr.2015.05.006

[8] Torki ME, Benzerga AA (2018) A mechanism of failure in shear bands. Extreme Mech Lett 23:67–71

[9] Fleck NA, Hutchinson JW, Tvergaard V (1989) Softening by void nucleation and growth in tension and shear. J Mech Phys Solids 37:515–540. https://doi.org/10.1016/0022-5096(89)90027-6

[10] Han G, He J, Li S, Lin Z (2024) Simple shear methodology for local structure-property relationships of sheet metals: State-of-the-art and open issues. Progress Mater Sci 143:101266. https://doi.org/10.1016/j.pmatsci.2024.101266

[11] Tomstad AJ, Frodal BH, Børvik T, Hopperstad OS (2022) Influence of particle content on the ductility of extruded non-recrystallized aluminium alloys subjected to shear loading. Mater Sci Eng A 850:143409

[12] Gross AJ, Ravi-Chandar K (2016) On the deformation and failure of Al 6061–T6 at low triaxiality evaluated through in situ microscopy. Int J Fract 200:185–208. https://doi.org/10.1007/s10704-016-0078-x

[13] Achouri M, Germain G, Dal Santo P, Saidane D (2013) Experimental characterization and numerical modeling of micromechanical damage under different stress states. Mater Des 50:207–222. https://doi.org/10.1016/j.matdes.2013.02.075

[14] Helfen L, Baumbach T, Mikulík P, Kiel D, Pernot P, Cloetens P, Baruchel J (2005) High-resolution three-dimensional imaging of flat objects by synchrotron-radiation computed laminography. Appl Phys Lett 86:071915

[15] Helfen L, Morgeneyer TF, Xu F, Mavrogordato MN, Sinclair I, Schillinger B, Baumbach T (2012) Synchrotron and neutron laminography for three-dimensional imaging of devices and flat material specimens. Int J Mater Res 2:170–173

[16] Kondori B, Morgeneyer TF, Helfen L, Benzerga AA (2018) Void growth and coalescence in a magnesium alloy studied by synchrotron radiation laminography. Acta Mater 155:80–94

[17] Buljac A, Helfen L, Hild F, Morgeneyer TF (2018) Effect of void arrangement on ductile damage mechanisms in nodular graphite cast iron: In situ 3D measurements. Eng Fract Mech 192:242–261

[18] Roth CC, Morgeneyer TF, Cheng Y, Helfen L, Mohr D (2018) Ductile damage mechanism under shear-dominated loading: In-situ tomography experiments on dual phase steel and localization analysis. Int J Plast 109:169–192

[19] Tancogne-Dejean T, Roth CC, Morgeneyer TF, Helfen L, Mohr D (2021) Ductile damage of aa2024-t3 under shear loading: Mechanism analysis through in-situ laminography. Acta Mater 205:116556

[20] Buljac A, Kong X, Helfen L, Hild F, Morgeneyer TF (2023) Shear loading dominated damage mechanisms and strain localization studied by in situ 3d laminography imaging and digital volume correlation for aa2198-t8. Mech Mater 178:104558. https://doi.org/10.1016/j.mechmat.2023.104558

[21] Kong X, Helfen L, Hurst M, Hänschke D, Missoum-Benziane D, Besson J, Baumbach T, Morgeneyer TF (2022) 3d in situ study of damage during a 'shear to tension' load path change in an aluminium alloy. Acta Mater 231:117842. https://doi.org/10.1016/j.actamat.2022.117842

[22] Morgeneyer TF, Besson J, Proudhon H, Starink MJ, Sinclair I (2009) Experimental and numerical analysis of toughness anisotropy in aa2139 al-alloy sheet. Acta Mater 57:3902–3915

[23] Kong X, Chen J, Madi Y, Missoum-Benziane D, Besson J, Morgeneyer T (2023) Plasticity and ductility of an anisotropic recrystallized AA2198 Al-Cu-Li alloy in T3 and T8 conditions during proportional and non-proportional loading paths: simulations and experiments . https://doi.org/10.46298/jtcam.8913 . https://jtcam.episciences.org/11078

[24] Hurst M, Helfen L, Morgeneyer TF, Suhonen H, Buljac A, Hild F, Suuronen J-P, Baumbach T, Hänschke D (2023) Hierarchically guided in situ nanolaminography for the visualisation of damage nucleation in alloy sheets. Sci Rep 13:1055. https://doi.org/10.1038/s41598-022-27035-8

[25] Martínez-Criado G, Villanova J, Tucoulou R, Salomon D, Suuronen JP, Labouré S, Guilloud C, Valls V, Barrett R, Gagliardini E, Dabin Y, Baker R, Bohic S, Cohen C, Morse J (2016) ID16B: a hard X-ray nanoprobe beamline at the ESRF for nanoanalysis. J Synchrotron Radiat 23:344–352

[26] Xu F, Helfen L, Suhonen H, Elgrabli D, Bayat S, Reischig P, Baumbach T, Cloetens P (2012) Correlative nanoscale 3d imaging of structure and composition in extended objects. PLoS ONE 7:50124. https://doi.org/10.1371/journal.pone.0050124

[27] Faragó T, Gasilov S, Emslie I, Zuber M, Helfen L, Vogelgesang M, Baumbach T (2022) Tofu: a fast, versatile and user-friendly image processing toolkit for computed tomography. J Synchrotron Radiat 29:916–927

[28] Hurst M (2024) Methodology for 4D X-ray microscopy and its application in material science. PhD thesis, Karlsruhe Institute of Technology (January). https://doi.org/10.5445/IR/1000167056

[29] Chen J (2011) Ductile tearing of AA2198 aluminium-lithium sheets for aeronautic application. Theses, École Nationale Supérieure des Mines de Paris (April)

[30] Petit T, Ritter C, Besson J, Morgeneyer TF (2018) Impact of machine stiffness on "pop-in" crack propagation instabilities. Eng Fract Mech 202:405–422. https://doi.org/10.1016/j.engfracmech.2018.08.007

[31] Rousselier G, Luo M (2014) A fully coupled void damage and mohr-coulomb based ductile fracture model in the framework of a reduced texture methodology. Int J Plasticity 55:1–24. https://doi.org/10.1016/j.ijplas.2013.09.002

[32] Kong X, Morgeneyer TF, Missoum-Benziane D, Rousselier G (2023) A polycrystalline damage model applied to an anisotropic aluminum alloy 2198 under non-proportional load path

changes. Int J Plast 168:103674. https://doi.org/10.1016/j.ijplas.2023.103674

[33] Besson J, Foerch R (1997) Large scale object-oriented finite element code design. Comput Methods Appl Mech Eng 142:165–187

Publisher's Note Springer Nature remains neutral with regard to jurisdictional claims in published maps and institutional affiliations.